Applied Catalysis B: Environmental 325 (2023) 122334

Contents lists available at ScienceDirect

Applied Catalysis B: Environmental

journal homepage: www.elsevier.com/locate/apcatb

Dual Ni active sites mediated by In to separate ethane activation and oxidation for enhanced ethene production via chemical looping scheme

Chaojie Wang [a,b], Ming Tian [a,*], Yujia Han [a,b], Teng Zong [a,b], Nanxin Wang [a,b], Lin Li [a], Jian Lin [a], Xiaodong Wang [a,*]

[a] CAS Key Laboratory of Science and Technology on Applied Catalysis, Dalian Institute of Chemical Physics, Chinese Academy of Sciences, 457 Zhongshan Road, Dalian 116023, People's Republic of China

[b] University of Chinese Academy of Sciences, 19(A) Yuquan Road, Shijingshan District, Beijing 100049, People's Republic of China

ARTICLE INFO

Keywords:
Chemical looping oxidative dehydrogenation
Main-group In
Electronic structure
Ethene adsorption
Selective oxidation

ABSTRACT

Chemical looping oxidative dehydrogenation (CL-ODH) opens a unique avenue to achieve highly efficient conversion of alkanes to value-added alkenes. The challenge lies in identical metal-oxo active sites responsible for both alkane activation and oxidation causing either insufficient activity or over-oxidation thus inferior ethene yield and productivity at relatively low temperature (< 650 °C). Herein, we designed a novel redox catalyst by the incorporation of main-group In (6NiIn$_x$/HY, x indicates the atomic ratio of In/Ni) which achieved more than 92 % ethene selectivity at 40 % ethane conversion and long-term stability at 600 °C with 0.22 mmol g^{-1} ethene productivity at 650 °C. This was because Ni^{2+} Lewis acid sites conducted catalytic dehydrogenation of ethane to ethene and hydrogen, and the Ni-O-In moiety outside HY framework enabled selective oxidation of hydrogen rather than ethene due to well-regulated Ni 3d electron densities leading to the reduction of adsorption for ethene thus decreasing over-oxidation.

1. Introduction

Ethene as one of the most important building blocks with global productivity capacity of more than 200 x 10^6 tons per year is used to produce a handful of polymers and specialty chemicals in chemical industry [1–3]. Typically, ethene is produced through steam cracking operated at very high temperature (1100 °C) which is a highly energy-intensive process with total energy demand of around 20 GJ t^{-1} in the case of naphtha as a feedstock [4–6]. A large amount of CO_2 (~1 ton/ton of ethene) and NO_x form due to the combustion of natural gas to supply sufficient heat, which raises considerably environmental concerns [6–9]. In addition, periodic reactor shut-down has to be required to remove coke formed on the inside reactor walls, leading to the increase in caption cost [5,6,9]. In contrast, oxidative dehydrogenation (ODH) is considered to be promising for the production of olefins by improving reaction efficiency because of favorable thermodynamics with energy savings of around 45% estimated without the problem of carbon deposition [1,2,10]. However, it also suffers from several challenges such as explosion risk due to co-feeding ethane and oxygen, capital-intensive air separation unit for oxygen source and inevitably consecutive oxidation to more thermodynamically stable CO and CO_2 (CO_x), limiting its practical industrial application [10–14]. Alternatively, chemical looping oxidative dehydrogenation (CL-ODH) of ethane takes advantage of lattice oxygen of redox catalysts to oxidize ethane to ethene and then the reduced redox catalysts are regenerated by air thus circumventing air separation and explosion concerns [3,6,15,16]. Moreover, active metal-oxo species can be elastically tuned to regulate their selectivity. Consequently, it is considered to be potential to surmount the shortcomings of traditional ODH and a promising candidate for highly efficient alkane utilization [17–31].

Redox catalysts which take on the activation of C-H bond in ethane and its selective oxidation play a pivotal role for CL-ODH [11,17,18]. Transition metal oxides with good ability for the ethane activation, high oxygen capacity and transport are ubiquitous and even have taken on the incarnations of redox catalysts in CL-ODH [4, 6, 9, 17–26]. Unfortunately, it is fraught since vast CO_x co-produced induced by that its lattice oxygen is usually reactive and facile to evolve into active but nonselective electrophilic oxygen species on the surface resulting in over-oxidation of ethene thus inferior selectivity [2,12,32,33]. To address the problem, researchers made extensive efforts to lower the

* Corresponding authors.
E-mail addresses: tm1982@dicp.ac.cn (M. Tian), xdwang@dicp.ac.cn (X. Wang).

https://doi.org/10.1016/j.apcatb.2022.122334
Received 23 August 2022; Received in revised form 15 December 2022; Accepted 27 December 2022
Available online 28 December 2022
0926-3373/© 2022 Elsevier B.V. All rights reserved.

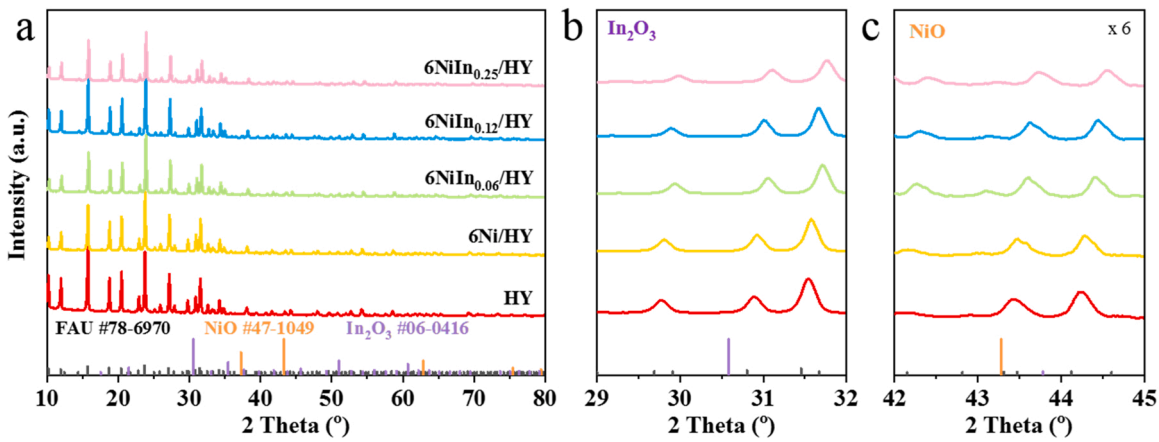

Fig. 1. (a) XRD pattern of fresh 6Ni/HY and 6NiIn$_x$/HY (x = 0.06, 0.12 and 0.25). (b, c) Enlarged XRD pattern in (a).

reactivity of lattice oxygen and enhance the resistance for O^{2-} diffusion from the bulk and its subsequent evolution into electrophilic oxygen species on the surface to improve ethene selectivity by the enhancement of binding energy of M-O bonds such as VO_x doped by Mo [11] and Fe_2O_3 doped by Co and Mo [24], and surface shielding of perovskites and Mg_6MnO_8 by inert $LiFeO_2$ [17], molten Na_2WO_4 [5,34] and Li_2CO_3 shell [9]. However, decreased oxygen reactivity brings about difficult activation for ethane so that higher reaction temperature (≥ 800 °C) is entailed to trigger CL-ODH, which results in thermal cracking thus obvious coke formation during the entire reduction process [3,5,24]. Moreover, the excessive passivation also causes low transport of lattice oxygen in turn quite limited oxygen (usually < 1 wt%) can be utilized for selective oxidation thus inferior ethene productivity [5,9,17,22,24]. Up to now, it is still challenging to achieve high ethene yield and productivity at relatively low temperature (< 650 °C) since both ethane activation and oxidation occurred on identical metal-oxo active sites resulting in either insufficient activity or over-oxidation. As a result, it can be more effective to design the redox catalysts with different active sites in charge of these two steps.

In the previous study, we designed dual Ni active sites by HY zeolite modification (xNi/HY, x ≤ 3 wt%) to separate ethane activation and oxidation wherein Ni^{2+} Lewis acid sites (LAS) conducted the activation of ethane leading to its catalytic dehydrogenation to C_2H_4 and H_2 while NiO nanoclusters confined in framework with lowered oxygen reactivity selectively oxidized H_2 generated rather than C_2H_4, which achieved near 100% ethene selectivity at relatively high ethane conversion for CL-ODH at lower temperature (600 °C) [35]. Unfortunately, ethene productivity is still unsatisfactory because of low amount of NiO inside HY framework (0.1 mmol g^{-1}), which impeded its practical application for CL-ODH. It is highly desired to further improve ethene production by increasing Ni loadings (higher oxygen storage capacity) but challenging because both ethane activation and oxidation would occur on the extremely active NiO outside zeolite framework leading to over-oxidation, as most transition metal oxides suffered from in CL-ODH [5, 6, 9, 11, 12, 17–25].

In as one of the main-group metals possesses unique electronic properties that its d-orbitals are fully occupied in comparison with transition metals [36–38], which could modulate electronic structure of NiO to reduce interaction between ethene and unoccupied d orbitals of Ni thus achieving selective oxidation. Herein, a novel redox catalyst modified by In (6NiIn$_x$/HY, x indicates the atomic ratio of In/Ni) was designed to separate ethane activation and oxidation for CL-ODH. Ni^{2+} LAS active sites conducted ethane activation and Ni-O-In species outside HY framework enabled selective oxidation of hydrogen rather than ethene due to increased electron density of Ni 3d reducing its adsorption. This afforded much better performance of 6NiIn$_{0.25}$/HY compared with state-of-the-art redox catalysts for CL-ODH without significant degradation during 105 redox cycles.

2. Experiment

2.1. Chemicals

Nickel (II) nitrate hexahydrate ($Ni(NO_3)_2{\cdot}6\ H_2O$, 98%) was purchased from Tianjin Damao Chemical Reagent Factory (Tianjin, China). Indium nitrate hydrate ($In(NO_3)_3{\cdot}xH_2O$, 99.99%) was purchased from Shanghai Macklin Biochemical Co., ltd. (Shanghai, China). HY with SiO_2/Al_2O_3 molar ratio of 5.4 (Sodium content < 0.8%) and NaY with SiO_2/Al_2O_3 molar ratio of 5.2 were obtained from Nankai University Catalyst Co., Ltd. (Tianjin, China).

2.2. Preparation of redox catalysts

All the HY or NaY-supported Ni samples with 6 wt% NiO loading were prepared by wetness impregnation method. Firstly, $Ni(NO_3)_2{\cdot}6\ H_2O$ (0.93 g) was dissolved into ultrapure water (3 mL) to obtain aqueous Ni precursor solution, and subsequently the impregnation was executed by adding HY or NaY zeolite. With the aid of ultrasonic, the obtained slurry was uniformly dispersed and dried at ambient temperature for 12 h. Subsequently, the samples were calcined at 720 °C for 6 h after dried at 60 °C and 120 °C for 12 h, respectively, and marked as 6Ni/HY and 6Ni/NaY. For the In ($In(NO_3)_3{\cdot}xH_2O$ served as the precursor of In) and Ni co-modified HY or NaY samples, co-impregnation method as mentioned above was used with the weight percentage of NiO fixed to 6 wt% and the atomic ratio of In/Ni of 0.06, 0.12 and 0.25. The aqueous Ni and In precursor solution were obtained by dissolving $Ni(NO_3)_2{\cdot}6\ H_2O$ and $In(NO_3)_3{\cdot}xH_2O$ into 3 mL ultrapure water. With the introduction of HY and NaY, the produced slurry was uniformly dispersed and dried at ambient temperature for 12 h. Similarly, the In doped Ni/HY or NaY samples were also calcined at 720 °C for 6 h after dried at 60 °C and 120 °C for 12 h, respectively, and named as 6NiIn$_x$/HY and 6NiIn$_x$/NaY, where x is the molar ratio of In/Ni. Moreover, 3Ni/HY-IE sample was prepared by nickel exchange procedure at 75 °C for 16 h using 100 mL of aqueous 0.01 M $Ni(NO_3)_2$ solution with 2 g HY as support. The exchanged product collected by filtration was washed with ultrapure water and dried at 80 °C for 12 h. Then, the obtained sample was well grinded and calcined at 500 °C for 4 h.

2.3. Characterization of redox catalysts

XRD pattern of 6Ni/HY and 6NiIn$_x$/HY were obtained by X′Pert-Pro powder X-ray diffractometer (PANalytical) equipped with Cu Kα monochromatized radiation (λ = 0.1541 nm, 40 kV, 40 mA). The data was collected on the 2θ range of 10–80° with a scanning speed of 1° min^{-1}.

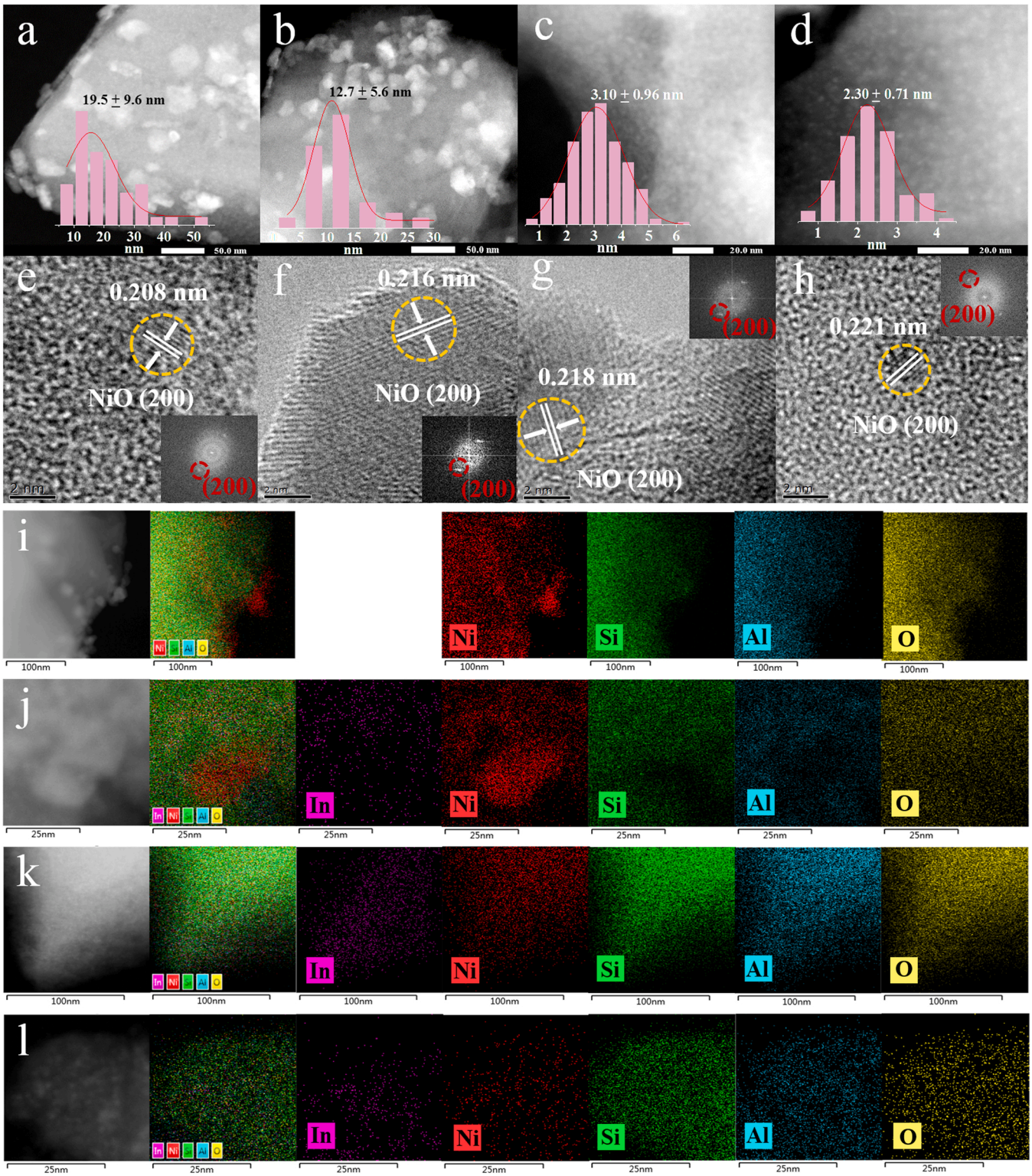

Fig. 2. (a-d) HAADF-STEM images, (e-h) HRTEM images and (i-l) EDS mappings of fresh 6Ni/HY and 6NiIn$_x$/HY (x = 0.06, 0.12 and 0.25), respectively.

The high-angle annular dark-field scanning transmission electron microscopy (HAADF-STEM), high-resolution transmission electron microscopy (HRTEM) and energy dispersive spectroscopy (EDS) of fresh, reduced and spent samples were performed with JEOL JEM-2100 F. Before microscopy characterization, the sample was ultrasonically dispersed in ethanol for 20 min, and then a drop of the suspension was dropped on a copper TEM grid coated with a thin holey carbon film.

The aberration-corrected (AC) HAADF-STEM images of atomically dispersed Ni^{2+} LAS for /HY-IE were obtained by a JEOL JEM-ARM200F with a CEOS probe corrector.

The X-ray absorption fine structure spectra (Ni K-edge) were collected at 4B9A beamline in Beijing Synchrotron Radiation Facility (BSRF). The storage rings of BSRF was operated at 2.5 GeV with a stable current of 400 mA. Using Si (111) double-crystal monochromator, the data collection was carried out in transmission mode. All spectra were collected in ambient conditions. For Wavelet Transform analysis, the

Table 1
EXAFS fitting results and parameters for 6Ni/HY and $6NiIn_{0.25}$/HY redox catalysts.

Sample	Shell	*CN*[a]	*R* (Å)[b]	σ^2 (Å^2)[c]	ΔE_0 (eV)[d]	*R* factor
Ni foil	Ni-Ni	12 *	2.483 ± 0.002	0.0061 ± 0.0002	7.3 ± 0.4	0.0023
NiO	Ni-O	6.2 ± 0.3	2.085 ± 0.010	0.0046 ± 0.0011	-1.4 ± 1.9	0.0059
	Ni-O-Ni	12.7 ± 0.9	2.948 ± 0.004	0.0059 ± 0.0004		
6Ni/HY	Ni-O	6.2 ± 0.5	2.047 ± 0.006	0.0052 ± 0.0008	-4.5 ± 1.1	0.0058
	Ni-O-Ni	2.7 ± 0.4	3.219 ± 0.022	0.0053 ± 0.0016		
$6NiIn_{0.25}$/HY	Ni-O	6.0 ± 0.5	2.048 ± 0.010	0.0060 ± 0.0006	1.8 ± 1.2	0.0148
	Ni-O-Ni	1.7 ± 0.6	3.085 ± 0.010	0.0081 ± 0.0057	0.9 ± 2.6	
	Ni-O-In	1.1 ± 0.3	3.402 ± 0.011			

R factor indicates the goodness of the fit. S_0^2 was fixed to 0.746, according to the experimental EXAFS fit of Ni foil by fixing *CN* as the known crystallographic value. * This value was fixed during EXAFS fitting, based on the known structure of Ni. Fitting range: $3.0 \le k$ (/Å) ≤ 13.9 and $1.0 \le R$ (Å) ≤ 3.0 (Ni foil); $3.0 \le k$ (/Å) ≤ 12.0 and $1.0 \le R$ (Å) ≤ 3.5 (Ni-1); $2.0 \le k$ (/Å) ≤ 11.5 and $1.0 \le R$ (Å) ≤ 3.5 (Ni-2). A reasonable range of EXAFS fitting parameters: $0.700 < S_0^2 < 1.000$; $CN > 0$; $\sigma^2 > 0$ Å^2; $|\Delta E_0| < 10$ eV; *R* factor < 0.02.

[a] *CN*, coordination number.
[b] *R*, the distance to the neighboring atom.
[c] σ^2, the Mean Square Relative Displacement (MSRD).
[d] ΔE_0, inner potential correction.

χ(k) exported from Athena was imported into the Hama Fortran code. The parameters were listed as follow: *R*-range, 1–4.0 Å, *k*-range, 0–13.0 Å^{-1} for sample (0–13.0 Å^{-1} for Ni foil and NiO); *k* weight, 2; and Morlet function with $\kappa = 10$, $\sigma = 1$ was used as the mother wavelet to provide the overall distribution.

Surface element analysis of samples was measured by XPS technique on a VG ESCALAB210 spectrometer with an Al Ka (hν = 1486.6 eV) X-ray source. The C1s peak at 284.8 eV was used as a reference to calibrate the binding energies of analyzed elements. For reduced samples, their Ni 2p3/2 spectra were detected in ex-situ condition but that of In 3d were measured in in-situ condition without exposed in air.

Pyridine adsorbed IR measurement was used to analyze and quantify the Brønsted and Lewis acid sites (BAS and LAS) in samples which were prepared into self-supporting wafers (25 mg, 14 mm (ID)) before experiment and then pretreated at 350 °C for 1 h in a home-made IR cell. When it came down to room temperature, degassed samples were treated with pyridine for 5 min at room temperature and then heated to 150 °C holding for 30 min under vacuum. IR spectra were collected by FT-IR spectrometer (Bruker, TENSOR 27) at room temperature and integrated to obtain the quantitative results of acid sites using molar extinction coefficients.

The specific surface area of HY, 6Ni/HY and $6NiIn_x$/HY (x = 0.06, 0.12 and 0.25) was measured with the Brunauer-Emmett-Teller (BET) equation and their pore volumes were estimated from the adsorption branches based on the t-plot method. Before the measurement, the samples were pretreated under vacuum at 300 °C for 8 h.

The Raman measurement of reduced 6Ni/HY and $6NiIn_x$/HY (x = 0.06, 0.12 and 0.25) at reaction condition were carried out on a LabRam HR800 confocal microprobe Raman instrument (HORIBA Jobin Yvon, France) equipped with laser excitation at 325 nm.

The difference of binding strength of M-O bond in 6Ni/NaY and $6NiIn_x$/NaY was investigated by temperature-programmed reaction (TPR) of H_2. The sample (200 mg) was loaded in fixed bed reactor and monotonously heated to 900 °C at a rate of 10 °C min^{-1} in gas atmosphere of 10% H_2/He (30 mL min^{-1}). Meanwhile, the residual H_2 in outlet gas was analyzed by an on-line mass spectrometry (MS).

The influence of incorporated In on the reaction behavior of M-O species in 6Ni/HY and $6NiIn_x$/HY was investigated by temperature-programmed reaction (TPR) of ethane in fixed bed reactor loading 200 mg samples. The reactor was monotonously heated to 700 °C at a rate of 5 °C min^{-1} in gas atmosphere of 10% C_2H_6/He (150 mL min^{-1}) while the composition of outlet gas was analyzed by an on-line FTIR (Bruker).

The adsorption strength and behavior of C_2H_6 or C_2H_4 on different metal-oxo species was studied by temperature-programmed desorption

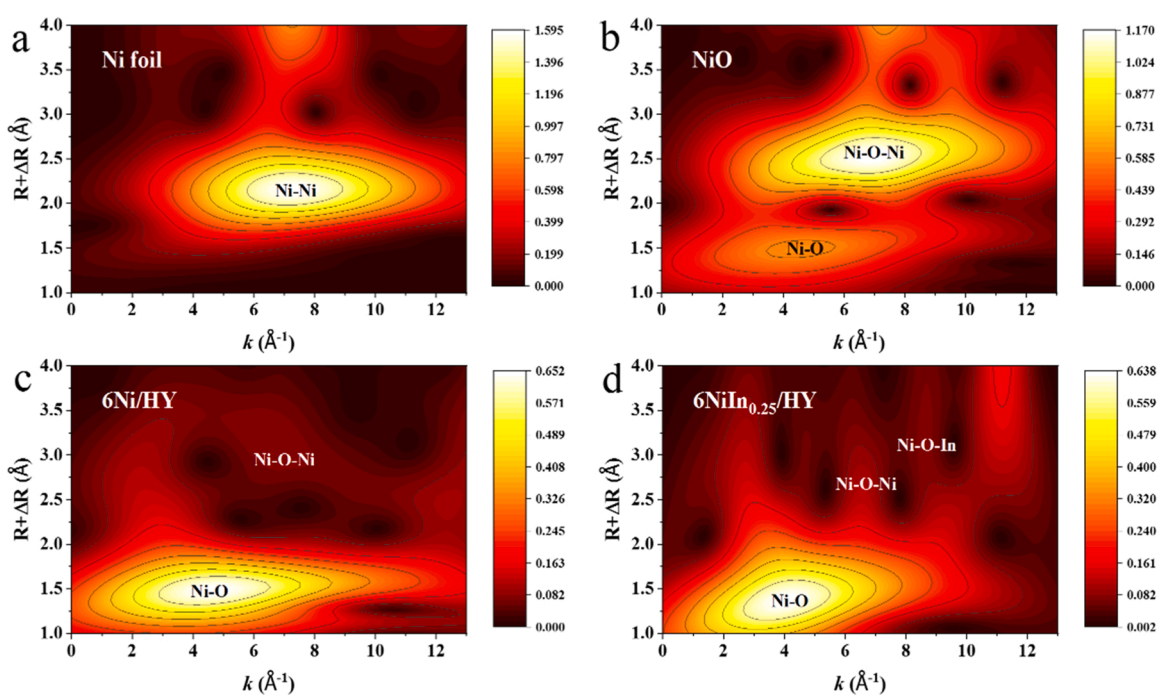

Fig. 3. Wavelet transform contour plots of (a) Ni foil, (b) NiO, (c) 6Ni/HY and (d) $6NiIn_{0.25}$/HY at nickel K-edge.

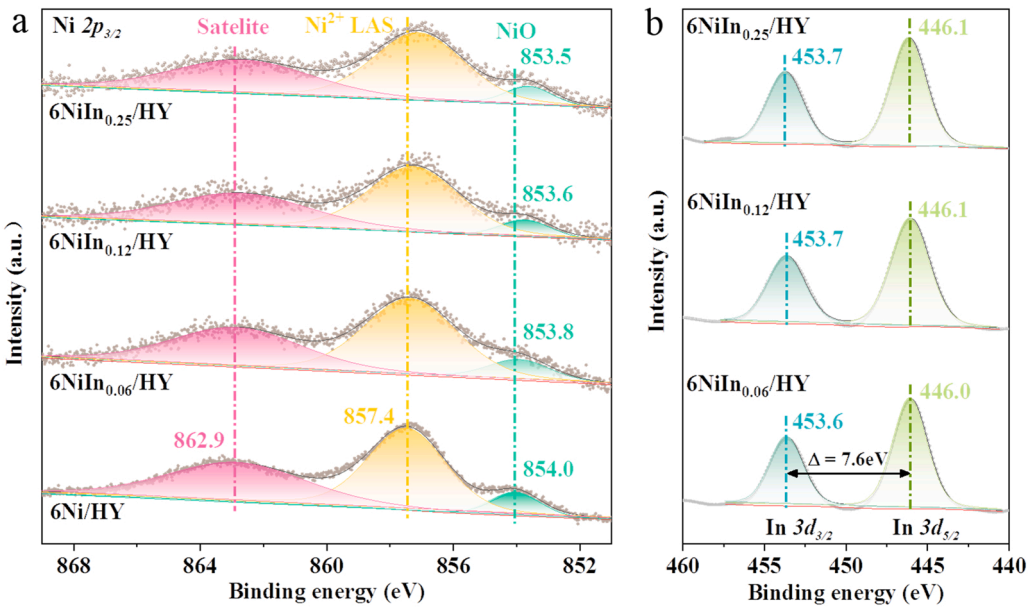

Fig. 4. (a) Ni $2p_{3/2}$ and (b) In *3d* spectra of fresh 6Ni/HY and 6NiIn$_x$/HY (x = 0.06, 0.12 and 0.25).

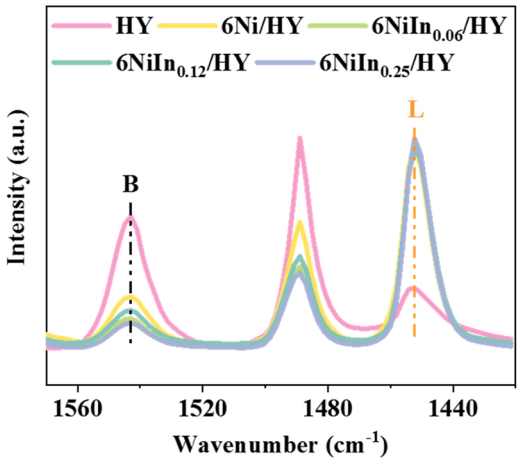

Fig. 5. Pyridine adsorbed FT-IR spectra of HY, 6Ni/HY and 6NiIn$_x$/HY (x = 0.06, 0.12 and 0.25). B and L stand for Brønsted and Lewis acid sites, respectively.

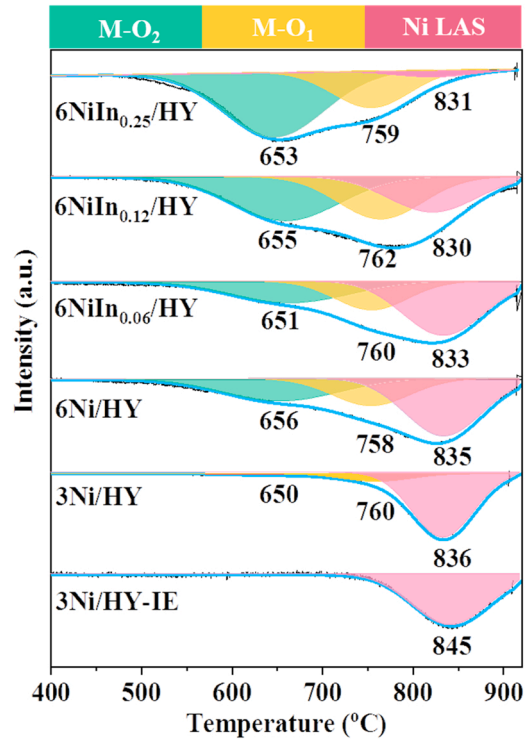

Fig. 6. H_2-TPR results of 3Ni/HY-IE, 3Ni/HY, 6Ni/HY and 6NiIn$_x$/HY (x = 0.06, 0.12 and 0.25). M-O_2 and M-O_1 stand for metal-oxo species outside and inside framework, respectively.

experiment on an Auto Chem II 2920 instrument and analyzed by matched mass spectrometry (MS). The pelleted samples were heated to 300 °C keeping for 1 h in a flow of He. After cooled to − 60 °C with liquid nitrogen and kept for 30 min to stabilize baseline, 5% C_2H_6/He with a volume of 0.7983 mL was introduced into the reactor in the form of pulse injection and lasted for 20 times in the interval of 2 min. After 30 min of purge and baseline stabilization in inert atmosphere (He), the reactor was monotonously heated to 700 °C at a rate of 10 °C min^{-1} while the composition of output exhaust gas was documented with mass spectrometer. The detected signals were 30, 26, 15, 44, 28, 2 and 18 m/e which corresponded to C_2H_6, C_2H_4, CH_4, CO_2, CO, H_2, and H_2O, respectively.

The H_2 and C_2H_4 cofeeding experiment of 6Ni/HY and 6NiIn$_x$/HY were performed with fixed bed reactor to study the oxidization difference for H_2 and C_2H_4 between NiO and In doped NiO nanoparticles. Firstly, the temperature of fixed bed reactor was raised to 650 °C and kept for 20 min in an inert atmosphere. Then, the gas atmosphere was switched to 1% H_2-1% C_2H_4/He (150 mL min^{-1}) and kept until no obvious change for H_2 and C_2H_4 composition. The on-line MS was used to quantify the consumption of H_2 and C_2H_4 during co-feeding process.

2.4. Performance of redox catalysts

Performance evaluation of redox catalysts were carried out in a quartz fixed-bed reactor (8 mm ID) loading 1.0 g samples (40–60 mesh) in each test. The reaction temperature for CL-ODH of ethane was typically 600 or 650 °C which was monitored by K-type thermocouple. Altering ethane and oxygen flows was employed in reaction process.

Table 2
Composition of metal-oxo species for 6Ni/HY and 6NiIn$_x$/HY (x = 0.06, 0.12 and 0.25).

Samples	Total M-O (μmol g^{-1})[a]	M-O$_2$ (μmol g^{-1})[b]	M-O$_1$ (μmol g^{-1})[c]	Ni^{2+} LAS (μmol g^{-1})[d]
6Ni/HY	903.00	232.08	202.70	468.22
6NiIn$_{0.06}$/HY	984.04	253.13	261.91	469.00
6NiIn$_{0.12}$/HY	1065.08	336.75	268.41	459.92
6NiIn$_{0.25}$/HY	1227.09	508.62	247.11	471.36

[a] Determined by ICP-AES analysis.
[b] Determined by actual consumption amount of H_2 for deconvoluted reduction peak at low temperature during H_2 TPR.
[c] Determined by subtracting the amount of Ni^{2+} LAS and M-O species outside (M-O$_2$) from that of total M-O.
[d] Determined by pyridine adsorbed FT-IR.

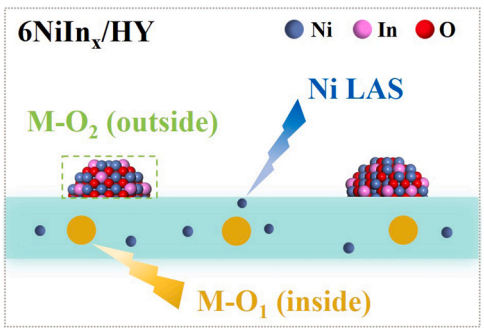

Fig. 7. Diagram of Ni species composition for 6NiIn$_x$/HY.

During reduction step, the redox catalysts were reduced for 1 min using 10% C_2H_6/He with a space velocity of 6500 h^{-1}. During oxidation step, the reduced redox catalysts were re-oxidized for 5 min using 5% O_2/He. Between the two steps, the reactor was purged using He with the flow rate of 200 mL min^{-1} for 2 min in order to restrain the mixing of ethane and oxygen. The results of activity test were not collected under kinetic conditions with no conspicuous mass transfer limitations.

The stability evaluation of 6NiIn$_{0.25}$/HY was performed for 105 cycles at 600 °C. The duration for reduction, re-oxidation and purging step was also set as 1 min, 5 min and 2 min thus lasting 10 min for a whole cycle process. The product composition in outlet streams was documented using an online IR analyzer (Bruker). The gas cell (25 mL) was heated to 30 °C before each test and the background spectrum was collected by the average of 30 scans. Software (MG01) provided by Bruker was used to analyze the collected spectra, and each species which include C_2H_6, C_2H_4, CH_4, CO, and CO_2 was quantified by picking its characteristic absorption band with excluding interference peaks from other species. Each data point was averaged by 3 scans (700–4000 cm^{-1} band at a resolution of 1 cm^{-1}) and the sampling interval between two data points was 0.7 s

The C_2H_6 conversion (Con) and C_2H_4 selectivity (Sel) (based on all products including formed coke and gas phase product) during whole reduction stage were defined as

$$\mathrm{Con}\,(\%) = \frac{\int_0^{t_{red}}\left[y_{C_2H_4} + \frac{1}{2}(y_{CH_4} + y_{CO} + y_{CO_2})\right]\mathrm{d}t + \frac{1}{2}\int_0^{t_{ox}}(y_{CO,\mathrm{ox}} + y_{CO_2,ox})dt}{\int_0^{t_{red}}\left[y_{C_2H_4} + y_{C_2H_6} + \frac{1}{2}(y_{CH_4} + y_{CO} + y_{CO_2})\right]\mathrm{d}t + \frac{1}{2}\int_0^{t_{ox}}(y_{CO,ox} + y_{CO_2,ox})dt} \times 100\% \tag{1}$$

$$\mathrm{Sel}\,(\%) = \frac{\int_0^{t_{red}} y_{C_2H_4}dt}{\int_0^{t_{red}}\left[y_{C_2H_4} + \frac{1}{2}(y_{CH_4} + y_{CO} + y_{CO_2})\right]dt + \frac{1}{2}\int_0^{t_{ox}}(y_{CO,ox} + y_{CO_2,ox})dt} \times 100\% \tag{2}$$

Where y_{C2H4}, y_{C2H6}, y_{CH4}, y_{CO2}, and y_{CO} are the composition of C_2H_4, C_2H_6, CH_4, CO_2, and CO in the outlet gas of the reduction step, respectively, $y_{CO,ox}$ and $y_{CO2,ox}$ are the composition of CO and CO_2 in the outlet gas of the re-oxidation step, respectively. In addition, t_{red} and t_{ox} are upper limit of integration which corresponds to the duration of reduction and oxidation step in the collected data, respectively. It should be emphasized that the integral time is not necessarily equal to feeding time due to the response of the analyzer and dead volume.

As Eq. (3) showed, C_2H_4 production was defined as the accumulative productivity of C_2H_4 within 1 min during the reduction stage.

$$\mathrm{Production}(\mathrm{mmol}\ g^{-1}) = \frac{F_{out} \times \int_0^{t_{red}} y_{C_2H_4}dt}{m \times V_m} \tag{3}$$

Where F_{out} is the total volume flow rate of outlet gas (mL s^{-1}), m is the loaded weight of redox catalyst (g), V_m stands for molar volume of gas at normal temperatures and pressures.

Space time yield (STY) of C_2H_4 was defined as the C_2H_4 productivity per unit catalyst weight per unit time.

$$\mathrm{STY}\ (\mathrm{mmol}\ g^{-1}) = \frac{F_{out} \times \int_0^{t_{red}} y_{C_2H_4}dt}{m \times V_m \times t_{fed}} \tag{4}$$

Where t_{fed} is the injection time of feed gas in reduction stage.

Oxygen utilization (O_e) is the ratio of actual oxygen consumption to total theoretically reducible lattice oxygen, which was calculated as

$$\mathrm{O_e}\ (\%) = \frac{F_{out} \times \int_0^{t_{red}}(y_{H_2O} + y_{CO} + 2y_{CO_2})\mathrm{d}t}{\sum x_i n_i m/M_i \times V_m \times 1000} \times 100\% \tag{5}$$

Where i stands for different metal oxide (NiO or In_2O_3). x_i is mass fraction of NiO or In_2O_3 in samples, n_i is stoichiometric ratio of oxygen in per mole of metal oxide, M_i is mole mass of metal oxide.

The overall carbon balance in reduction stage was defined as

$$\mathrm{Carbon}\ balance\ (\%) = \frac{\mathrm{Total\ carbon}\ detected}{\mathrm{Total\ carbon}\ fed} \times 100\%$$

$$= \frac{F_{out} \times \left\{\int_0^{t_{red}}\left[y_{C_2H_4} + y_{C_2H_6} + \frac{1}{2}\left(y_{CH_4} + y_{CO} + y_{CO_2}\right)\right]dt + \frac{1}{2}\int_0^{t_{ox}}\left(y_{CO,ox} + y_{CO_2,ox}\right)dt\right\}}{F_{in} \times y_{in,C_2H_6} \times t_{fed}} \times 100 \tag{6}$$

Where $y_{in,C2H6}$ is the composition of C_2H_6 in the inlet gas, F_{in} is the total volume flow rate (mL s^{-1}) of inlet gas.

The H_2 and C_2H_4 consumption (Cons) under co-feeding condition for 6NiIn$_x$/HY (x = 0.06, 0.12 and 0.25) were obtained by the integral of corresponding MS quantitative results, which was denoted as

$$\mathrm{Cons}\ (\mathrm{mmol}\ g^{-1}) = \frac{F_{in} \times t_{fed} \times y_{fed,i} - F_{out} \times \int_0^{t_{red}} y_i dt}{m \times V_m} \tag{7}$$

Where i stands for different gas component (H_2 or C_2H_4), F_{in} and F_{out} are the flow rate of inlet and outlet gas (mL s^{-1}), respectively, t_{fed} is the intake time of cofeeding gas (1% C_2H_4 and 1% H_2), $y_{fed,i}$ is the volume fraction of H_2 or C_2H_4 at the inlet, y_i is the volume fraction of H_2 or C_2H_4 in the effluent gas, m is the initial weight of samples (g), V_m is molar volume of gas at normal temperatures and pressures.

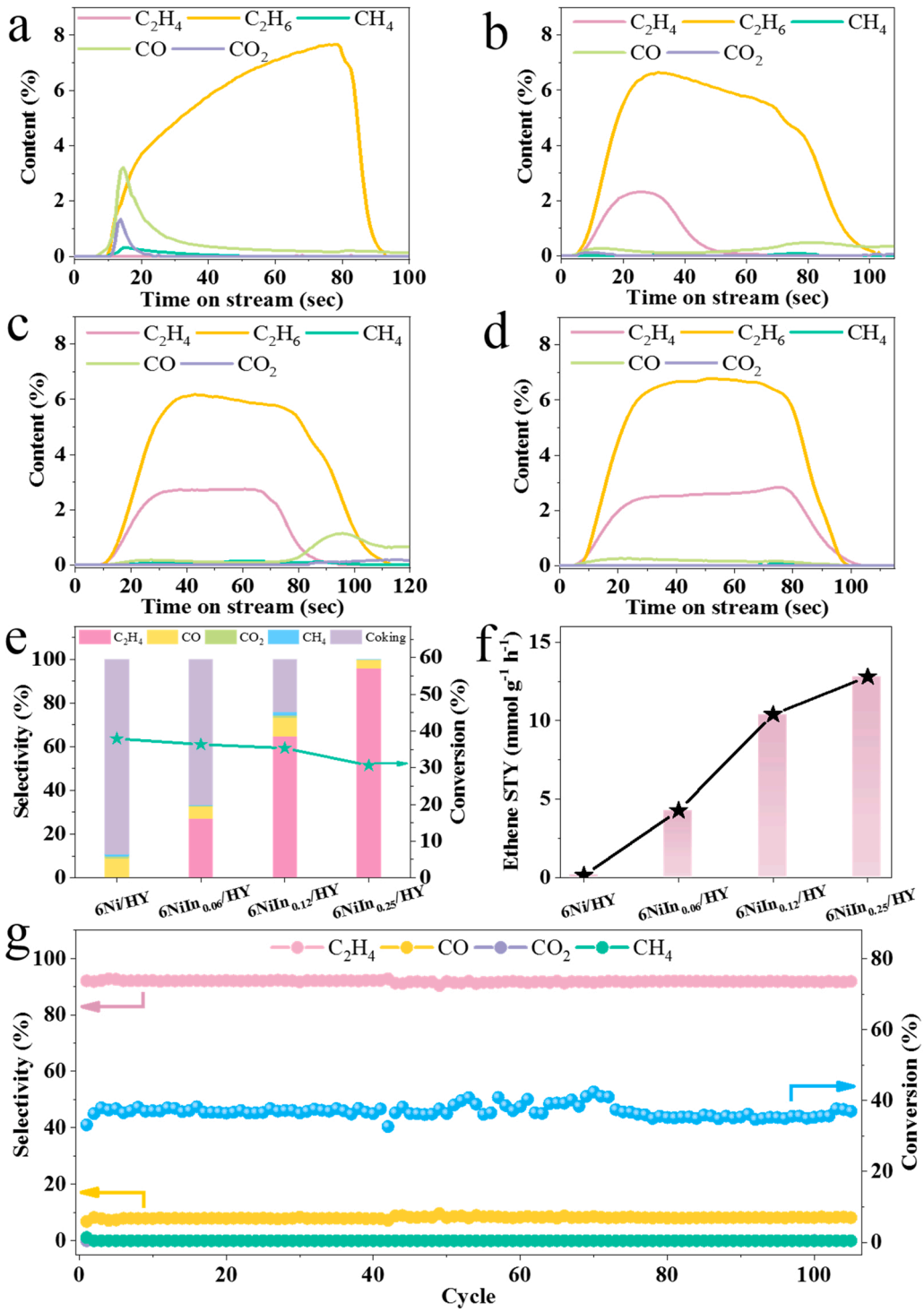

Fig. 8. (a-d) Reaction kinetic profile during reduction stage, (e) products distribution and ethane conversion and (f) ethene STY over 6Ni/HY and $6NiIn_x/HY$ (x = 0.06, 0.12 and 0.25) at 650 °C with space velocity of 24000 h^{-1} and 6500 h^{-1}, respectively. (g) Stability test of $6NiIn_{0.25}/HY$ under reaction condition of 600 °C and 700 h^{-1} space velocity.

3. Results and discussion

3.1. Structure analysis of redox catalysts

To get insight into the structure evolution of In incorporated Ni/HY ($6NiIn_x/HY$, x denotes the mole ratio of In/Ni), a series of characterization was executed. The results of textural properties of fresh samples showed that BET surface area and pore volume hardly changed with In loadings (Table S1). It could be seen in XRD results of 6Ni/HY and $6NiIn_x/HY$ (Fig. 1) that only diffraction peaks ascribed to NiO centred at 43° (PDF No. 47–1049) [33] and FAU structure for HY zeolite (PDF No. 78–6970) [39] were observed without those of In_2O_3 (Fig. 1b) [40], indicating that NiO was present outside HY framework and incorporated In was highly dispersed. HAADF-STEM results showed that there were some aggregated nanoparticles with a d-spacing of 0.208 nm attributed to NiO (200) outside framework of HY zeolite for 6Ni/HY (Fig. 2a, e and i), which was consistent with XRD results (Fig. 1c) [33]. For $6NiIn_x/HY$, aggregated NiO nanoparticles were still observed but the lattice plane

Table 3
Performance comparison between $6NiIn_{0.25}/HY$ redox catalyst and previously reported results for CL-ODH of ethane.

Redox catalyst	Cat/C_2H_6 concentration (g)	GHSV (h^{-1})	T (°C)	Conversion (%)	Selectivity (%)	Production (mmol g^{-1})	Space time yield (mmol g^{-1} h^{-1})	Oxygen utilization (%)[a]	Reference
NaW-Mg_6MnO_8	0.6	4500	800	38.7	91.4	0.12	2.4	4.10	[5]
Li-LaSrFeO	1.3	3000	650	31.8	95.2	0.001	0.06	1.41	[17]
Li_2CO_3-LaSrFeO	40–6.3	480	650	35.0	95.0	/	/	4.71	[9]
MoO_3/Fe_2O_3	0.6	1500	600	6.4	59.3	0.02	0.4	0.87	[21]
$Co_{0.3}Mo_{0.7}/Fe_2O_3$	5.6	6000	775	21.0	84.0	0.05	3.0	2.27	[24]
VO_x/Al_2O_3-ZrO_2	0.4	/	600	37.9	90.0	0.03	2.7	/	[19]
$0.2Ce/SrFeO_3$	2.8	3000	725	29.0	82.0	0.24	4.11	2.58	[22]
FeO_x/TiO_2	5	/	550	9.7	91.1	/	4.66	/	[4]
3Ni/HY	10	5100	600	18	99	0.05	0.05	39.20	[35]
$6NiIn_{0.25}/HY$	10	700	600	42.4	91.5	0.03	1.80	3.82	This work
$6NiIn_{0.25}/HY$	10	3300	600	13.8	98.9	0.06	3.34	4.50	This work
$6NiIn_{0.25}/HY$	10	6500	600	8.2	99.8	0.07	4.20	4.55	This work
$6NiIn_{0.25}/HY$	10	6500	650	31.7	95.8	0.22	13.2	19.12	This work

[a] Determined by actual oxygen consumption divided by theoretically reducible oxygen capacity.

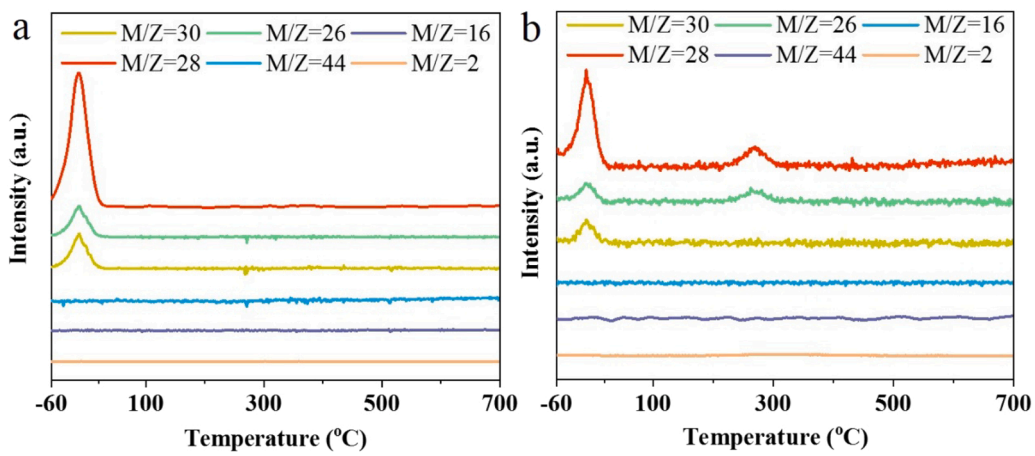

Fig. 9. Ethane TPD over (a) $6NiIn_{0.25}/NaY$ and (b) $6NiIn_{0.25}/HY$.

spacing for NiO (200) was slightly expanded with the increase of In loading, hinting that In should be implanted into lattice of NiO nanoparticles outside (Fig. 2e-h). In order to further confirm the formation of Ni-O-In, we performed X-ray absorption fine structure (XAFS) characterization to analyze the secondary coordination layer information of NiO [41–43]. As seen in Fig. S1 and Table 1, the Fourier transform (FT) of extended X-ray absorption fine structure (EXAFS) of Ni K-edge and the fitting results showed that the coordination number of Ni-O-Ni (~3.2 Å) was 2.7 for 6Ni/HY while the secondary coordination number for $6NiIn_{0.25}/HY$ was around 2.8 with Ni-O-Ni of 1.7 at about 3.1 Å and Ni-O-In of 1.1 at about 3.4 Å (Fig. S1 and Table 1) [44–46]. In addition, the wavelet transformed plot of $6NiIn_{0.25}/HY$ was significantly different from that of 6Ni/HY (Fig. 3) and further demonstrated the Ni-O-In species formed via substituting 39.3% Ni by In [42,46]. Extensive study commonly focused on the influence of dopants on the binding energy of M-O bonds and reducibility [11,22,24,47,48]. To the best of our knowledge, their effect on the electronic structure of transition metal oxides has been few studied in CL-ODH. Thus, X-ray photoelectron spectroscopy (XPS) of 6Ni/HY and $6NiIn_x/HY$ was carried out. As shown in Fig. 4a, the binding energies of Ni 2p for $6NiIn_x/HY$ prominently shifted toward more negative values than that of 6Ni/HY with shifting extent increasing with In loadings, suggesting that the incorporation of In increased the electron density of Ni cation for NiO nanoparticles outside with less vacant d-states via formed Ni-O-In bonds (Fig. S2). This might reduce ethene re-adsorption owing to the weakened bond between Ni and electron-rich group of C=C because of electrostatic repulsion thus avoiding continuous oxidation [49].

EDS mappings presented that some well distributed Ni species with Si, Al and O elements could be also observed besides aggregated NiO for 6Ni/HY (Fig. 2a, e and i). Pyridine adsorbed Fourier transform infrared (FTIR) spectra (Fig. 5) showed that Ni^{2+} LAS generated by substituting the proton of BAS reflected by significantly decreased BAS (1543 cm^{-1}) and increased LAS (1452 cm^{-1}) [50], which indicated the presence of Ni^{2+} LAS besides NiO nanoparticles outside HY framework for 6Ni/HY. For $6NiIn_x/HY$, Ni and In species also distributed well with Si, Al, O elements besides aggregated In-doped NiO ones (Fig. 2j-l), and co-impregnation of Ni and In also resulted in remarkable decrease for BAS (1543 cm^{-1}) while increase in LAS (1452 cm^{-1}) in comparison with those of HY in pyridine adsorbed FTIR spectra (Fig. 5), indicating the existence of metal LAS. However, it is difficult to distinguish which metals were anchored as isolated metal species with more than one metal precursor. Given that the electronic property of metal centres is significantly affected by its coordination environment inducing change in its binding energy, XPS would be instrumental to ascertain isolated metal species. As shown in Fig. 4a, one peak at about 857 eV ascribed to Ni^{2+} LAS in HY [35,51,52] was observed besides those at around 854 eV and 863 eV attributed to NiO and its satellite peak [33,52], respectively, for $6NiIn_x/HY$. Nevertheless, only one kind of In species existed in $6NiIn_x/HY$ with its peaks positioned at around 446 eV and 453 eV ascribed to In_2O_3 without those at higher binding energy attributed to In

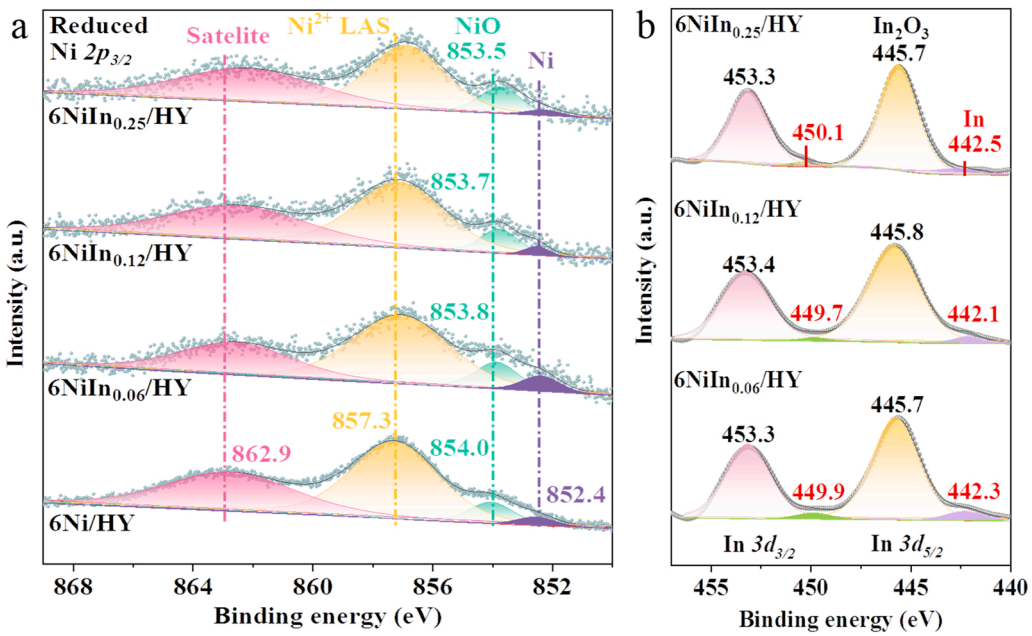

Fig. 10. (a) Ni $2p_{3/2}$ and (b) In *3d* spectra of reduced 6Ni/HY and 6NiIn$_x$/HY (x = 0.06, 0.12 and 0.25) under reaction condition of 650 °C and 6500 h^{-1} space velocity.

LAS (Fig. 4b) [53]. Additionally, quantitative results of pyridine adsorbed FTIR showed almost the same metal LAS content even though mole ratio of In/Ni increased from 0.06 to 0.25 for 6NiIn$_x$/HY compared with 6Ni/HY (Table S1). These results manifested that only Ni precursor engaged in ion exchange with protons of BAS in HY leading to the exclusive formation of Ni^{2+} LAS for 6NiIn$_x$/HY. This also obeyed to the fact that lower content, and weaker exchange capacity of In due to larger ion radius than that of Ni greatly reduced the possibility that In was anchored as LAS [54].

In order to quantify Ni^{2+} LAS, NiO and In-doped NiO nanoparticles, temperature-programmed reaction of H_2 (H_2-TPR) characterization of 6Ni/HY and 6NiIn$_x$/HY as well as 3Ni/HY-IE with only Ni^{2+} LAS, and 3Ni/HY with Ni^{2+} LAS and NiO nanoparticles inside HY framework without NiO nanoparticles outside was carried out (Figs. S3 –5 and Table S2). For 6Ni/HY, three reduction peaks could be observed by deconvoluting the H_2 consumption peak (Fig. 6). Compared with 3Ni/HY-IE and 3Ni/HY reference samples (Fig. 6), the reduction peak from the lowest to highest temperature could be attributed to the reduction of NiO nanoparticles outside, inside HY framework and Ni^{2+} LAS in sequence. For 6NiIn$_x$/HY, the reduction peak of NiO nanoparticles outside significantly enhanced and the extent was more obvious with increased In loadings, indicating that larger amount of In doped into NiO nanoparticles outside to form Ni-O-In species (Table S3). It should be noted that the amount of Ni^{2+} LAS determined in H_2-TPR was much lower than that in pyridine adsorbed FTIR spectra for all the samples (Table S1 and Table S3). This was because the isolated Ni species co-ordinated with framework O could not be completely reduced to rebuild the BAS (Si-(OH)-Al) due to the diffusion resistance for H_2 inside framework and its weaker dissociation for H_2 than that of aggregated counterparts [55]. The same held for NiO nanoparticles confined into framework due to its strong interaction with HY zeolite. As a result, the amount of Ni^{2+} LAS and NiO nanoparticles inside framework were determined by pyridine adsorbed FTIR spectra and subtracting that of Ni^{2+} LAS and NiO nanoparticles outside from that of actual M-O, respectively, and their amount were given in Table 2. Taken together, Ni^{2+} LAS, NiO nanoparticles inside and Ni-O-In moiety outside HY framework with enhanced electron density of Ni cation probably reducing ethene adsorption were present in 6NiIn$_x$/HY as shown in Fig. 7, which might separate ethane activation and selective oxidation thus achieving high ethene yield and productivity. This differed from the state-of-the-art redox catalysts in CL-ODH of ethane where these two steps usually took place on identical metal-oxo active site resulting in either insufficient activity or consecutive oxidation.

3.2. Catalytic performance of redox catalysts

The performance of CL-ODH of ethane over 6Ni/HY and 6NiIn$_x$/HY with altering ethane and O_2 was evaluated to examine the promoting effect of In incorporation. It could be seen from the evolution profiles of gas product for 6Ni/HY at 650 °C (Fig. 8a) in which negligible C_2H_4 could be observed with remarkable signals of CH_4 and CO_x, presenting quite low ethene selectivity, productivity, space time yield (STY) and coke formation (Fig. 8e, f) during reduction stage proved by Raman spectra (Fig. S6) with obvious D and G bands signals centred at 1410 and 1580 cm^{-1}, respectively [11,12]. This should be because both ethane activation and oxidation occurred on active NiO nanoparticles outside HY zeolite leading to over-oxidization and cracking (Figs. 1, 2a, e, i, S6 and S7c), as shown in the most transition metal oxides reported before [3,5,9,11,17,23–25]. Contrastively, the incorporation of In gave rise to a positive effect embodied in the obvious production of ethene and alleviation of over-oxidation during reduction stage, and the promotional function became more prominent with the increase of In introduction (Fig. 8b-e). This could be further demonstrated by the results of temperature-programmed reaction (TPR) of ethane as shown in Fig. S8, where the co-production of CO_x significantly decreased with the In incorporation. As a result, the higher ethene selectivity were achieved for 6NiIn$_x$/HY than that of plain 6Ni/HY and 6NiIn$_{0.25}$/HY with the largest In/Ni mole ratio of 0.25 exhibited the most optimal performance with the instantaneous ethene selectivity of close to 100% (Fig. S9d) and cumulative selectivity of up to 96%, respectively, during the overall reduction process (Fig. 8e). Moreover, different from most of the state-of-the-art redox catalysts reported for CL-ODH of ethane in which high ethene selectivity usually sacrificed active lattice oxygen leading to limited oxygen utilization thus inferior ethene productivity and high reaction temperature [5,24,34], the oxygen utilization, ethene STY and productivity of 6NiIn$_{0.25}$/HY reached as large as 19%, 13.2 mmol g^{-1} h^{-1} and 0.22 mmol g^{-1}, respectively, almost one or two magnitude higher than most redox catalysts reported previously with comparable

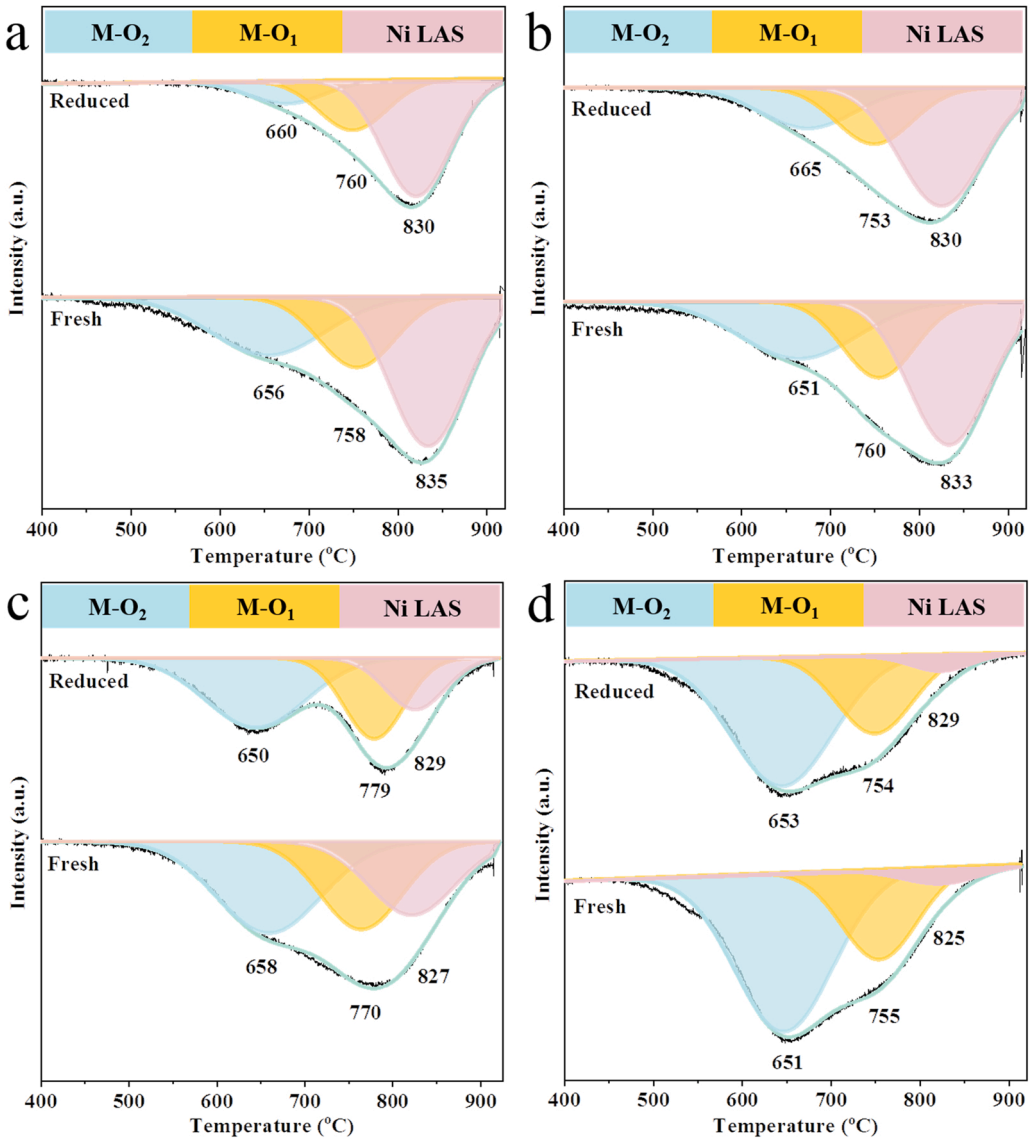

Fig. 11. Comparison of H_2 TPR results for fresh and reduced (a) 6Ni/HY and (c-d) 6NiIn$_x$/HY (x = 0.06, 0.12 and 0.25). M-O$_2$ and M-O$_1$ stand for metal-oxo species outside and inside framework, respectively.

Table 4
Consumption of metal-oxo species outside (M-O$_2$) and inside (M-O$_1$) during C_2H_6 reduction process.

Samples	M-O$_2$ (μmol g^{-1})[a]	M-O$_1$ (μmol g^{-1})[a]
6Ni/HY	177.51	53.54
6NiIn$_{0.06}$/HY	126.01	47.28
6NiIn$_{0.12}$/HY	102.55	82.40
6NiIn$_{0.25}$/HY	113.97	44.93

[a] Determined by subtracting the amount of corresponding metal-oxo species of reduced samples obtained via H_2-TPR results from that of fresh samples.

conversion even at relatively lower temperature (Fig. 8f and Table 3). This indicated that different active sites in the designed redox catalysts modified by In might undertake ethane activation and oxidation achieving highly efficient CL-ODH, which should be related with the tuned electronic structure of NiO nanoparticles outside by In incorporation (Fig. 4a and Fig. S2) thus reducing its interaction with ethene.

To verify the stability of In incorporated redox catalysts during repeated dehydrogenation-regeneration cycles, a stability evaluation was carried out on 6NiIn$_{0.25}$/HY. As shown in Fig. 8g, few changes of product distribution in the total dehydrogenation step were observed during 105 redox cycles, indicating that the excellent stability of performance of 6NiIn$_{0.25}$/HY for CL-ODH of ethane. STEM and EDS mapping characterization results of reduced 6NiIn$_{0.25}$/HY (Fig. S10) showed almost identical size distribution of partially reduced NiO nanoparticles without obvious sintering compared with fresh those. More importantly, no visible damage of framework structure (Fig. S11), near invariable amount of Ni^{2+} LAS (Fig. S12) and good element distribution for Ni and In without apparent In separation from NiO lattice (Fig. S13) after 105 redox cycles further manifested that unchanged structure and composition of active sites in 6NiIn$_x$/HY should be responsible for its long-term stable performance.

3.3. Discussion

3.3.1. Dual active sites mediated by In to separate ethane activation and oxidation

It is challenging to regulate identical active sites to realize both ethane activation and selective oxidation thus high ethene yield and productivity for CL-ODH, e.g. high reactivity resulted in over-oxidation as 6Ni/HY and 6Ni/NaY (Fig. 8a and S7c) showed or inferior one led to

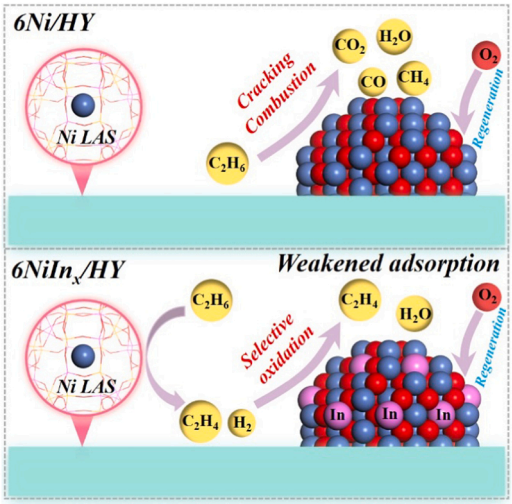

Scheme 1. Schematic illustration of the promotion effect of incorporated In on enhancing the catalytic performance of Ni/HY redox catalyst.

insufficient activity. In the present work, the over-oxidation was inhibited concurrently with remarkably increased production of ethene with increase of In/Ni from 0.06 to 0.25 (Fig. 8 and Figs. S8, 9), and $6NiIn_{0.25}$/HY exhibited comparable ethene yield and superior ethene productivity even at lower temperature without obvious carbon deposition (Fig. S6 and Table 3). These results indicated that ethane activation and selective oxidation should occur on different active sites of In-modified 6Ni/HY. In order to identify active sites for the activation of ethane over $6NiIn_{0.25}$/HY, a reference sample of $6NiIn_{0.25}$/NaY was prepared wherein only In-modified NiO species were present (Fig. S14) without Ni^{2+} LAS due to the absence of BAS in NaY leading to that Ni^{2+} LAS could not be produced by substituting the pronons of BAS [35,56]. Fig. 9a, b presents ethane TPD of $6NiIn_{0.25}$/NaY and $6NiIn_{0.25}$/HY. For $6NiIn_{0.25}$/NaY, no desorption peaks of C_2H_6 and its evolutive products were observed even when the temperature reached 700 °C in addition to that at low temperature (< −10 °C) ascribed to the weak adsorption of C_2H_6 (Fig. 9a), indicating that In-modified NiO species with the formation of Ni-O-In bonds weakly interacted with ethane and exhibited inferior activity for CL-ODH of ethane (Fig. S15). In comparison, new peaks appeared at higher temperature (about 270 °C) for $6NiIn_{0.25}$/HY (Fig. 9b) which could be ascribed to the desorption of ethene formed via the C-H activation of strongly adsorbed ethane, intensively confirming that Ni^{2+} LAS enabled the activation and dehydrogenation of C_2H_6.

The metal-oxo species of $6NiIn_x$/HY participating in CL-ODH of ethane would be identified. XPS results showed that the peak ascribed to Ni^0 at around 852.4 eV for all the reduced $6NiIn_x$/HY samples was observed (Fig. 10a) and the amount of normalized M-O species evidently decreased from about 40.3–30.5% (Fig. S16d) for $6NiIn_{0.25}$/HY [35,52], manifesting definite contribution of lattice oxygen during the CL-ODH process. In order to determine which kind of oxygen species participated in ethane reduction, H_2-TPR of reduced samples was carried out and compared with that of fresh ones. It could be found in Fig. 11 and Table S4 that the amount of H_2 consumption for both metal-oxo species inside and outside HY framework decreased and the declined amount of the latter was almost 2–3 times of that of the former for $6NiIn_x$/HY (Table 4), indicating that In-modified NiO nanoparticles outside principally participated in the CL-ODH of ethane. This could be further confirmed by XPS results of reduced samples in which In^0 positioned at around 442 eV was observed (Fig. 10b) [53]. Thus, the improved ethene selectivity of $6NiIn_x$/HY should originate from Ni-O-In moiety for

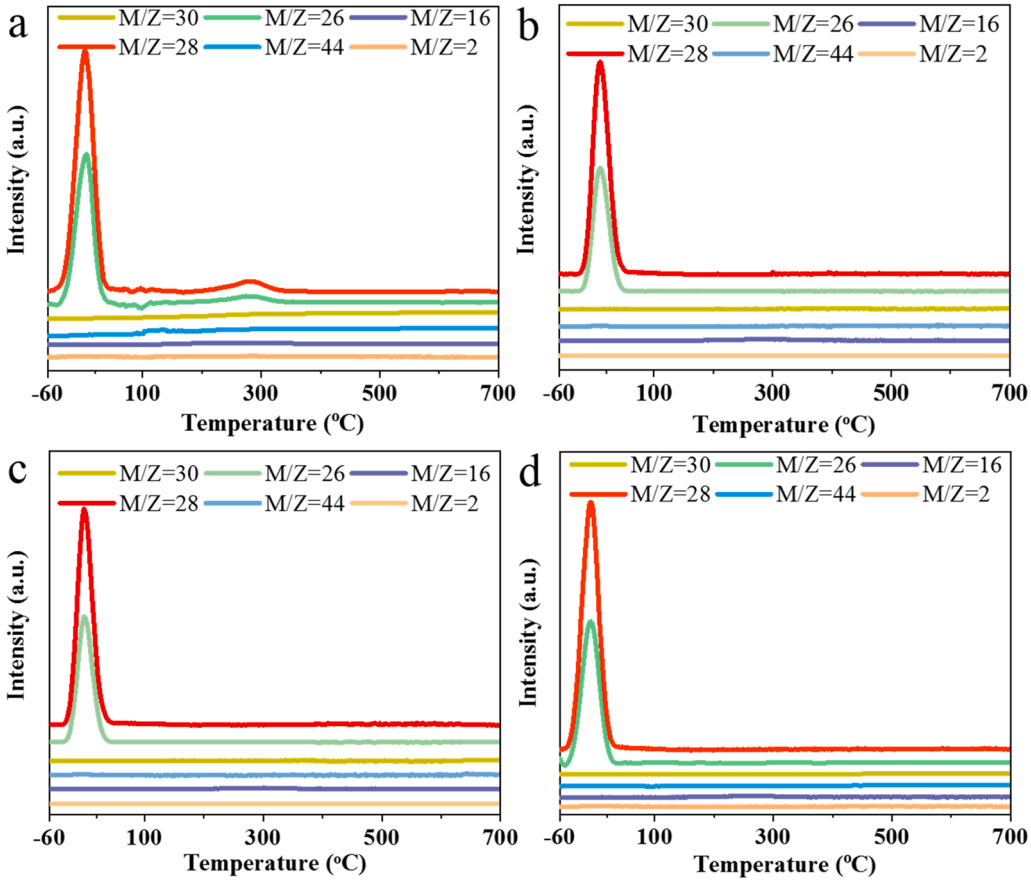

Fig. 12. Ethene TPD over (a) 6Ni/NaY and (b-d) $6NiIn_x$/NaY (x = 0.06, 0.12 and 0.25).

selective oxidation of hydrogen formed on Ni^{2+} LAS. This could be supported by co-feeding experiment of C_2H_4 and H_2 for $6NiIn_x/HY$ wherein the consumption amount of H_2 was about 4–33 times as many as C_2H_4 (Fig. S17b-d, S18 and Table S5).

As a result, dual active sites of Ni^{2+} LAS and Ni-O-In moiety outside HY framework with the help of In separated ethane activation and selective oxidation, which was responsible for high ethene STY yield and productivity of $6NiIn_{0.25}/HY$ without coke formation at relatively lower temperature, as summarized in Scheme 1.

3.3.2. Insight into the essence of In incorporation

It was well accepted that selective H_2 oxidation of metal-oxo species was relevant to the enhanced M-O binding strength by the doped foreign promotors in chemical looping field [6,11,22,24,47]. Rare research studied the impact of dopants on the electronic structure of M-O and adsorption behaviour for ethene. To insight into the essence of selective H_2 oxidation of Ni-O-In moiety, the H_2-TPR and C_2H_4 TPD were performed. As shown in Fig. S19, hydrogen consumption peaks were centred at almost the same temperature with no shift to higher temperature for $6NiIn_x/NaY$ compared with 6Ni/NaY. This indicated that Ni-O bonding strength were not visibly enhanced with the formation of Ni-O-In bonds and it should be irrelevant with selective H_2 oxidation of Ni-O-In moiety in current study. On the contrary, it could be seen that the desorption peak at about 280 °C attributed to stronger adsorbed ethene in comparison with those at about 0 °C for 6Ni/NaY (Fig. 12a) disappeared with the incorporation of In (Fig. 12b-d), indicating that incorporated In could effectively weaken the adsorption of ethene on NiO nanoparticles outside HY framework. Moreover, the concomitantly derived CO_2 signals during ethene TPD for $6NiIn_x/NaY$ dramatically lowered even disappeared with the increase of In incorporation in contrast to that for 6Ni/NaY (Fig. S20), further demonstrating the weakened adsorption and interaction between ethene and Ni-O-In moiety. This should be ascribed to electronic interaction between Ni and incorporated In that the electron transferred from In to Ni reducing the vacancy of d-states of Ni via formed Ni-O-In bonds thus interaction of Ni and electron-rich group of C═C of ethene because of electrostatic repulsion (Fig. 4a and Fig. S2), which accounted for selective H_2 oxidation of Ni-O-In moiety outside HY framework. This provided a new way to design redox catalysts with dual active sites by modifying electronic structure of metal-oxo species to achieve selective oxidation for CL-ODH.

4. Conclusion

In summary, consecutive oxidation of $6NiIn_x/HY$ was remarkably inhibited with increase in the In loadings and $6NiIn_{0.25}/HY$ exhibited the best performance with more than 92% ethene selectivity at 40% ethane conversion and long-term stability at 600 °C, and 0.22 mmol g^{-1} ethene productivity with over 19% oxygen utilization at 650 °C, almost one magnitude larger than the redox catalyst reported previously for CL-ODH of ethane. Multiple characterization results indicated that Ni was present in the form of Ni^{2+} LAS, NiO nanoparticles inside and Ni-O-In moiety outside HY framework which triggered the electron transferring from In to Ni. Ni^{2+} LAS conducted the activation of ethane and the formed Ni-O-In species with the weakened adsorption for ethene induced by increased electron density of Ni cations endowed the selective oxidation of H_2 rather than ethene, which achieved highly efficient CL-ODH of ethane. This study demonstrated an approach to improve ethene yield and productivity of redox catalysts for CL-ODH by designing dual active sites to separate ethane activation and oxidation and modifying electronic structure of metal-oxo species to weaken ethene adsorption, which paved a completely new route toward the design of high-performance redox catalysts.

CRediT authorship contribution statement

Chaojie Wang: Investigation, Reaction tests, Characterization, Writing – original draft. **Ming Tian:** Supervision, Draft review and editing. **Yujia Han:** Characterization, Data curation. **Teng Zong:** Data curation, Methodology. **Nanxin Wang:** Investigation, Reaction tests. **Lin Li:** Resources. **Jian Lin:** Conceptualization, Methodology, Funding acquisition. **Xiaodong Wang:** Supervision, Conceptualization, Methodology, Draft review and editing, Funding acquisition.

Declaration of Competing Interest

The authors declare that they have no known competing financial interests or personal relationships that could have appeared to influence the work reported in this paper.

Data Availability

No data was used for the research described in the article.

Acknowledgements

We are grateful for the financial support provided by the National Natural Science Foundation of China (NSFC) grants (22178337) and Dalian Science Foundation for Distinguished Young Scholars (2021RJ10). The authors sincerely thank Yang Su for the useful discussion of HRTEM and HAADF-STEM characterizations.

Appendix A. Supporting information

Supplementary data associated with this article can be found in the online version at doi:10.1016/j.apcatb.2022.122334.

References

[1] J.T. Grant, J.M. Venegas, W.P. McDermott, I. Hermans, Aerobic oxidations of light alkanes over solid metal oxide catalysts, Chem. Rev. 118 (2018) 2769–2815.
[2] C.A. Gärtner, A.C. vanVeen, J.A. Lercher, Oxidative dehydrogenation of ethane: common principles and mechanistic aspects, Chem. Cat. Chem. 5 (2013) 3196–3217.
[3] S. Yusuf, V. Haribal, D. Jackson, L. Neal, F. Li, Mixed iron-manganese oxides as redox catalysts for chemical looping–oxidative dehydrogenation of ethane with tailorable heat of reactions, Appl. Catal. B Environ. 257 (2019), 117885.
[4] M.H. Jeong, J. Sun, G.Y. Han, D.H. Lee, J.W. Bae, Successive reduction-oxidation activity of FeO_x/TiO_2 for dehydrogenation of ethane and subsequent CO_2 activation, Appl. Catal. B Environ. 270 (2020), 118887.
[5] S. Yusuf, L.M. Neal, F. Li, Effect of promoters on manganese-containing mixed metal oxides for oxidative dehydrogenation of ethane via a cyclic redox scheme, ACS Catal. 7 (2017) 5163–5173.
[6] X. Zhu, Q. Imtiaz, F. Donat, C.R. Muller, F.X. Li, Chemical looping beyond combustion - a perspective, Energy Environ. Sci. 13 (2020) 772–804.
[7] B. Sarkar, R. Goyal, L.N. Sivakumar Konathala, C. Pendem, T. Sasaki, R. Bal, MoO_3 nanoclusters decorated on TiO_2 nanorods for oxidative dehydrogenation of ethane to ethylene, Appl. Catal. B Environ. 217 (2017) 637–649.
[8] Y.S. Yun, M. Lee, J. Sung, D. Yun, T.Y. Kim, H. Park, K.R. Lee, C.K. Song, Y. Kim, J. Lee, Y.-J. Seo, I.K. Song, J. Yi, Promoting effect of cerium on MoVTeNb mixed oxide catalyst for oxidative dehydrogenation of ethane to ethylene, Appl. Catal. B Environ. 237 (2018) 554–562.
[9] Y. Gao, X. Wang, J. Liu, C. Huang, K. Zhao, Z. Zhao, X. Wang, F. Li, A molten carbonate shell modified perovskite redox catalyst for anaerobic oxidative dehydrogenation of ethane, Sci. Adv. 6 (2020) eaaz9339.
[10] J.T. Grant, C.A. Carrero, F. Goeltl, J. Venegas, P. Mueller, S.P. Burt, S.E. Specht, W. P. McDermott, A. Chieregato, I. Hermans, Selective oxidative dehydrogenation of propane to propene using boron nitride catalysts, Science 354 (2016) 1570–1573.
[11] S. Chen, L. Zeng, R. Mu, C. Xiong, Z.J. Zhao, C. Zhao, C. Pei, L. Peng, J. Luo, L. S. Fan, J. Gong, Modulating lattice oxygen in dual-functional Mo-V-O mixed oxides for chemical looping oxidative dehydrogenation, J. Am. Chem. Soc. 141 (2019) 18653–18657.
[12] S. Chen, C. Pei, X. Chang, Z.J. Zhao, R. Mu, Y. Xu, J. Gong, Coverage-dependent behaviors of vanadium oxides for chemical looping oxidative dehydrogenation, Angew. Chem. Int. Ed. 59 (2020) 22072–22079.
[13] J. Liu, Z. Zhang, Y. Jiang, X. Jiang, N. He, S. Yan, P. Guo, G. Xiong, J. Su, G. Vilé, Influence of the zeolite surface properties and potassium modification on the Zn-catalyzed CO_2-assisted oxidative dehydrogenation of ethane, Appl. Catal. B Environ. 304 (2022), 120947.

[14] J. Sheng, W.C. Li, W.D. Lu, B. Yan, B. Qiu, X.Q. Gao, R.P. Zhang, S.Z. Zhou, A.H. Lu, Preparation of oxygen reactivity-tuned FeO_x/BN catalyst for selectively oxidative dehydrogenation of ethylbenzene to styrene, Appl. Catal. B Environ. 305 (2022), 121070.

[15] Y. Kang, Y.J. Han, M. Tian, C.D. Huang, C.J. Wang, J. Lin, B.L. Hou, Y. Su, L. Li, J. H. Wang, X.D. Wang, Promoted methane conversion to syngas over Fe-based garnets via chemical looping, Appl. Catal. B Environ. 278 (2020), 119305.

[16] W.D. Sun, G.F. Zhao, Y. Gao, J.Q. Si, Y. Liu, Y. Lu, An oxygen carrier catalyst toward efficient chemical looping-oxidative coupling of methane, Appl. Catal. B Environ. 304 (2022), 120948.

[17] Y. Gao, L.M. Neal, F. Li, Li-promoted $La_xSr_{2-x}FeO_{4-\delta}$ core–shell redox catalysts for oxidative dehydrogenation of ethane under a cyclic redox scheme, ACS Catal. 6 (2016) 7293–7302.

[18] L. Zeng, Z. Cheng, J.A. Fan, L.S. Fan, J.L. Gong, Metal oxide redox chemistry for chemical looping processes, Nat. Rev. Chem. 2 (2018) 349–364.

[19] A.H. Elbadawi, M.S. Ba-Shammakh, S. Al-Ghamdi, S.A. Razzak, M.M. Hossain, H. I. de Lasa, A fluidizable VO_x/γ–Al_2O_3–ZrO_2 catalyst for the ODH of ethane to ethylene operating in a gas phase oxygen free environment, Chem. Eng. Sci. 145 (2016) 59–70.

[20] I.M. Gerzeliev, A.Y. Popov, V.A. Ostroumova, Oxidative dehydrogenation of ethane to ethylene in a system with circulating microspherical metal oxide oxygen carrier: 2. Ethylene production in a pilot unit with a riser reactor, Pet. Chem. 56 (2016) 724–729.

[21] P. Novotný, S. Yusuf, F. Li, H.H. Lamb, Oxidative dehydrogenation of ethane using MoO_3/Fe_2O_3 catalysts in a cyclic redox mode, Catal. Today 317 (2018) 50–55.

[22] X. Tian, C. Zheng, H. Zhao, Ce-modified $SrFeO_{3-\delta}$ for ethane oxidative dehydrogenation coupled with CO_2 splitting via a chemical looping scheme, Appl. Catal. B Environ. 303 (2022), 120894.

[23] T. Wang, Y. Gao, Y. Liu, M. Song, J. Liu, Q. Guo, Core-shell $Na_2WO_4/CuMn_2O_4$ oxygen carrier with high oxygen capacity for chemical looping oxidative dehydrogenation of ethane, Fuel 303 (2021), 121286.

[24] X. Tian, C. Zheng, F. Li, H. Zhao, Co and Mo co-doped Fe_2O_3 for selective ethylene production via chemical looping oxidative dehydrogenation, ACS Sustain. Chem. Eng. 9 (2021) 8002–8011.

[25] G. Luongo, F. Donat, A.H. Bork, E. Willinger, A. Landuyt, C.R. Muller, Highly selective oxidative dehydrogenation of ethane to ethylene via chemical looping with oxygen uncoupling through structural engineering of the oxygen carrier, Adv. Energy Mater. 12 (2022) 2200405.

[26] A.A. Ayandiran, I.A. Bakare, H. Binous, S. Al-Ghamdi, S.A. Razzak, M.M. Hossain, Oxidative dehydrogenation of propane to propylene over VO_x/CaO–γ-Al_2O_3 using lattice oxygen, Catal. Sci. Technol. 6 (2016) 5154–5167.

[27] K. Kousi, D. Neagu, L. Bekris, E. Papaioannou, I.S. Metcalfe, Endogenous nanoparticles strain perovskite host lattice providing oxygen capacity and driving oxygen exchange and CH_4 conversion to syngas, Angew. Chem. Int. Ed. 59 (2020) 2510–2519.

[28] Y. Liu, L. Qin, Z. Cheng, J.W. Goetze, F. Kong, J.A. Fan, L.S. Fan, Near 100% CO selectivity in nanoscaled iron-based oxygen carriers for chemical looping methane partial oxidation, Nat. Commun. 10 (2019) 5503.

[29] M.S.C. Chan, E. Marek, S.A. Scott, J.S. Dennis, Chemical looping epoxidation, J. Catal. 359 (2018) 1–7.

[30] R.B. Dudek, X. Tian, M. Blivin, L.M. Neal, H. Zhao, F. Li, Perovskite oxides for redox oxidative cracking of n-hexane under a cyclic redox scheme, Appl. Catal. B Environ. 246 (2019) 30–40.

[31] D. Li, R. Xu, X. Li, Z. Li, X. Zhu, K. Li, Chemical looping conversion of gaseous and liquid fuels for chemical production: a review, Energy Fuels 34 (2020) 5381–5413.

[32] D. Dogu, K.E. Meyer, A. Fuller, S. Gunduz, D.J. Deka, N. Kramer, A.C. Co, U. S. Ozkan, Effect of lanthanum and chlorine doping on strontium titanates for the electrocatalytically-assisted oxidative dehydrogenation of ethane, Appl. Catal. B Environ. 227 (2018) 90–101.

[33] Y. Zhou, J. Lin, L. Li, M. Tian, X. Li, X. Pan, Y. Chen, X. Wang, Improving the selectivity of Ni-Al mixed oxides with isolated oxygen species for oxidative dehydrogenation of ethane with nitrous oxide, J. Catal. 377 (2019) 438–448.

[34] W. Ding, K. Zhao, S. Jiang, Z. Zhao, Y. Cao, F. He, Alkali-metal enhanced $LaMnO_3$ perovskite oxides for chemical looping oxidative dehydrogenation of ethane, Appl. Catal. A. Gen. 609 (2021), 117910.

[35] C. Wang, B. Yang, Q. Gu, Y. Han, M. Tian, Y. Su, X. Pan, Y. Kang, C. Huang, H. Liu, X. Liu, L. Li, X. Wang, Near 100% ethene selectivity achieved by tailoring dual active sites to isolate dehydrogenation and oxidation, Nat. Commun. 12 (2021) 5447.

[36] P.P. Power, Main-group elements as transition metals, Nature 463 (2010) 171–177.

[37] S. Liu, Z. Li, C. Wang, W. Tao, M. Huang, M. Zuo, Y. Yang, K. Yang, L. Zhang, S. Chen, P. Xu, Q. Chen, Turning main-group element magnesium into a highly active electrocatalyst for oxygen reduction reaction, Nat. Commun. 11 (2020) 938.

[38] C. Wang, Y. Han, M. Tian, L. Li, J. Lin, X. Wang, T. Zhang, Main-group catalysts with atomically dispersed In sites for highly efficient oxidative dehydrogenation, J. Am. Chem. Soc. 144 (2022) 16855–16865.

[39] H. Awala, J.P. Gilson, R. Retoux, P. Boullay, J.M. Goupil, V. Valtchev, S. Mintova, Template-free nanosized faujasite-type zeolites, Nat. Mater. 14 (2015) 447–451.

[40] H.C. Xu, Y. Wang, X.L. Dong, N. Zheng, H.C. Ma, X.F. Zhang, Fabrication of In_2O_3/In_2S_3 microsphere heterostructures for efficient and stable photocatalytic nitrogen fixation, Appl. Catal. B Environ. 257 (2019), 117932.

[41] B. Ravel, M. Newville, ATHENA, ARTEMIS, HEPHAESTUS: data analysis for X-ray absorption spectroscopy using IFEFFIT, J. Synchrotron Rad. 12 (2005) 537–541.

[42] H. Funke, A.C. Scheinost, M. Chukalina, Wavelet analysis of extended x-ray absorption fine structure data, Phys. Rev. B 71 (2005), 094110.

[43] S.I. Zabinsky, J.J. Rehr, A. Ankudinov, R.C. Albers, M.J. Eller, Multiple-scattering calculations of x-ray-absorption spectra, Phys. Rev. B 52 (1995) 2995–3009.

[44] C. Xiao, L. Cheng, Y. Zhu, G. Wang, L. Chen, Y. Wang, R. Chen, Y. Li, C. Li, Super-coordinated nickel $N_4Ni_1O_2$ site single-atom catalyst for selective H_2O_2 electrosynthesis at high current densities, Angew. Chem. Int. Ed. 61 (2022), e202206544.

[45] Y. Zhou, A.J. Martín, F. Dattila, S. Xi, N. López, J. Pérez-Ramírez, B.S. Yeo, Long-chain hydrocarbons by CO_2 electroreduction using polarized nickel catalysts, Nat. Catal. 5 (2022) 545–554.

[46] T. Yan, N. Li, L. Wang, W. Ran, P.N. Duchesne, L. Wan, N.T. Nguyen, L. Wang, M. Xia, G.A. Ozin, Bismuth atom tailoring of indium oxide surface frustrated Lewis pairs boosts heterogeneous CO_2 photocatalytic hydrogenation, Nat. Commun. 11 (2020) 6095.

[47] C. Jiang, H. Song, G. Sun, X. Chang, S. Zhen, S. Wu, Z.J. Zhao, J. Gong, Data-driven interpretable descriptors for the structure-activity relationship of surface lattice oxygen on doped vanadium oxides, Angew. Chem. Int. Ed. 61 (2022) e202206758.

[48] E. Heracleous, A.A. Lemonidou, Ni–Me–O mixed metal oxides for the effective oxidative dehydrogenation of ethane to ethylene – effect of promoting metal Me, J. Catal. 270 (2010) 67–75.

[49] P. Yin, X. Luo, Y. Ma, S.Q. Chu, S. Chen, X. Zheng, J. Lu, X.J. Wu, H.W. Liang, Sulfur stabilizing metal nanoclusters on carbon at high temperatures, Nat. Commun. 12 (2021) 3135.

[50] C.A. Emeis, Determination of integrated molar extinction coefficients for infrared-absorption bands of pyridine adsorbed on solid acid catalysts, J. Catal. 141 (1993) 347–354.

[51] Y. Chai, G. Wu, X. Liu, Y. Ren, W. Dai, C. Wang, Z. Xie, N. Guan, L. Li, Acetylene selective hydrogenation catalyzed by cationic nickel confined in zeolite, J. Am. Chem. Soc. 141 (2019) 9920–9927.

[52] M. Akri, S. Zhao, X. Li, K. Zang, A.F. Lee, M.A. Isaacs, W. Xi, Y. Gangarajula, J. Luo, Y. Ren, Y.T. Cui, L. Li, Y. Su, X. Pan, W. Wen, Y. Pan, K. Wilson, L. Li, B. Qiao, H. Ishii, Y.F. Liao, A. Wang, X. Wang, T. Zhang, Atomically dispersed nickel as coke-resistant active sites for methane dry reforming, Nat. Commun. 10 (2019) 5181.

[53] M.M. Li, H. Zou, J. Zheng, T.S. Wu, T.S. Chan, Y.L. Soo, X.P. Wu, X.Q. Gong, T. Chen, K. Roy, G. Held, S.C.E. Tsang, Methanol synthesis at a wide range of H_2/CO_2 ratios over a Rh-In bimetallic catalyst, Angew. Chem. Int. Ed. 59 (2020) 16039–16046.

[54] J.J. Chen, K. Giewont, E.A. Walker, J. Lee, Y. Niu, E.A. Kyriakidou, Cobalt-induced PdO formation in low-loading Pd/BEA catalysts for CH_4 oxidation, ACS Catal. 11 (2021) 13066–13076.

[55] L. Kuai, Z. Chen, S. Liu, E. Kan, N. Yu, Y. Ren, C. Fang, X. Li, Y. Li, B. Geng, Titania supported synergistic palladium single atoms and nanoparticles for room temperature ketone and aldehydes hydrogenation, Nat. Commun. 11 (2020) 48.

[56] I. Friberg, N. Sadokhina, L. Olsson, The effect of Si/Al ratio of zeolite supported Pd for complete CH_4 oxidation in the presence of water vapor and SO_2, Appl. Catal. B Environ. 250 (2019) 117–131.